Supplementary material

Assessing global-scale organic matter reactivity patterns in marine sediments using a lognormal reactive continuum model

Sinan Xu[1,2], Bo Liu[2], Sandra Arndt[3], Sabine Kasten[2,4], Zijun Wu[1*]

[1]*State Key Laboratory of Marine Geology, School of Ocean and Earth Science, Tongji University, Shanghai, 200092, P.R. China*

[2]*Alfred Wegener Institute Helmholtz Centre for Polar and Marine Research, 27570 Bremerhaven, Germany*

[3]*Department of Geosciences, Environment and Society, Universit´e Libre de Bruxelles, Avenue Franklin Roosevelt 50, 1050 Brussels, Belgium*

[4]*Faculty of Geosciences, University of Bremen, 28359 Bremen, Germany*

1. Distribution of sites and calculation of sedimentation rate

1.1 Distribution map of sites analyzed in this paper.

We selected the sedimentary OM data distributed on the global shelf, slope and abyss sediments, and fitted the OM depth-profiles with the lognormal RCM (Fig. S1). The detailed information of these sites is shown in the Table S4.

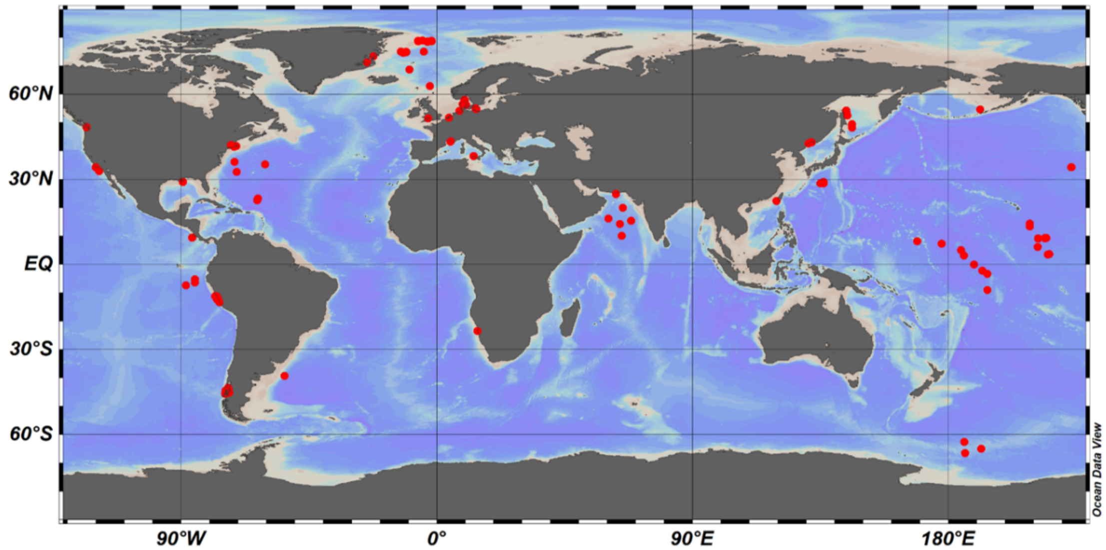

Fig. S1. Global distribution of investigated sites. The red dots are the location of the site. These sediment cores include gravity, multiple corer or others coring device. Considering the simulation analysis requires sediment core data from the sea-water interface (SWI) to the bottom of the sediment (the major length of the samples analyzed in the paper ranges from 10cm to 1000cm), the number of sites collected is limited, while they still cover the shelf, slopes and abyss regions.

1.2 Empirical formula of ocean water depth and sedimentation rate.

We collected sedimentation rate data in surface sediment at more than 600 sites(Arndt et al., 2013; Betts and Holland, 1991; Colman and Holland, 2000; Egger et al., 2018; Seiter et al., 2004), and chose the model as following (equation (S1)) from (Burwicz et al., 2011).

$$\omega = \frac{w1}{1+(\frac{z}{z1})^{c1}} + \frac{w2}{1+(\frac{z}{z2})^{c2}} \quad \text{(S1)}$$

when $w1$=0.1, $z1$=200, $c1$=3.3, $w2$=0.001, $z2$=4500, $c2$=11.4, the best fitting effect is obtained shown as Fig. S2.

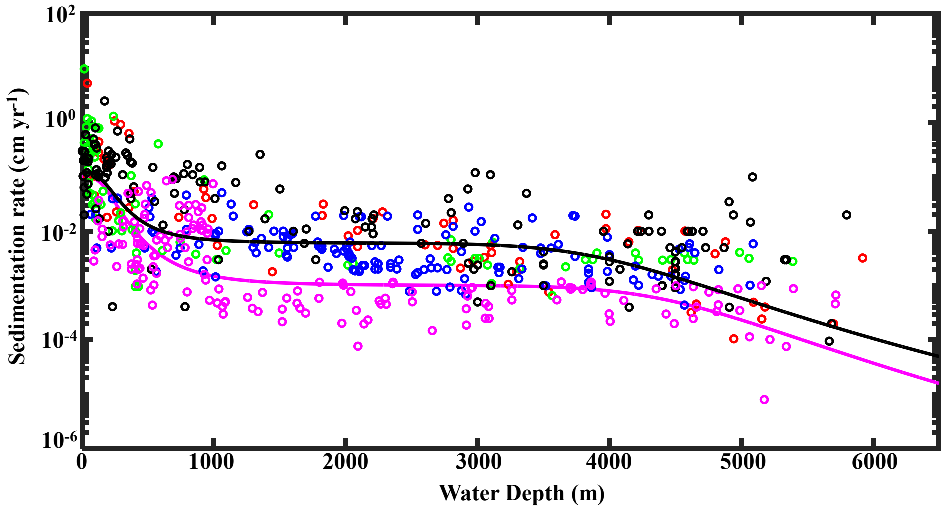

Fig. S2. Sedimentation rate (*w*) as a function of water depth (*z*). The date taken from (Arndt et al., 2013), (Egger et al., 2018), (Betts and Holland, 1991), (Colman and Holland, 2000), and (Seiter et al., 2004) are shown as black, pink, red, green and blue circles. The pink line is the fitting result, defined as equation (S1) (R^2=0.57). The black line is obtained from Burwicz et al., 2001 (R^2=0.43).

2. Comparison of fitting results between gamma-RCM and lognormal-RCM

We compared the fitting results of gamma RCM (γ-RCM) and lognormal RCM (l-RCM) through eight sites of sediment OM depth-profiles (Boudreau and Ruddick, 1991) (Fig. S3). The coefficient of determination (R^2) is an index that evaluates fitting results (Table S1).

Table S1. List of model parameters and coefficients of determination (R^2) for the fitting result of γ-RCM and l-RCM.

Core	γ-RCM			l-RCM		
	v	a	R^2	μ	σ	R^2
Foam	0.152	4.2	0.930	2.2×10^{-3}	3.725	0.923
SCR-44	0.202	70.4	0.929	4.4×10^{-4}	2.706	0.922
BX-6	0.278	22.5	0.929	2.24×10^{-3}	2.031	0.936
PC2&TW2	0.052	0.16	0.937	5.5×10^{-5}	6.688	0.947
10141&2	0.193	10184	0.935	1.9×10^{-6}	3.289	0.936
7706-41K	0.910	141.3	0.974	9.5×10^{-3}	0.899	0.972
7706-36	0.804	231.7	0.978	4.79×10^{-4}	1.089	0.980
DSDP58	1.080	20224	0.917	6.11×10^{-5}	1.663	0.921

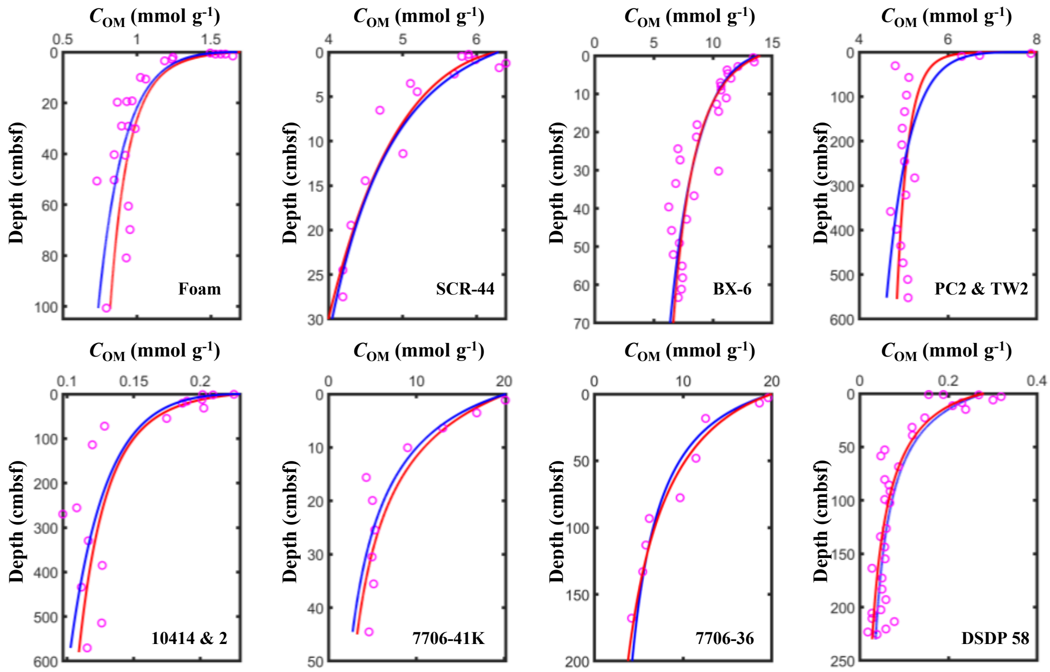

Fig. S3. Fitting results of *l*-RCM and *γ*-RCM. The pink dots are the measured OM data, the red lines are *l*-RCM fitting results, and the blue lines are *γ*-RCM fitting results.

3. Parameter sensitivity analysis for *l*-RCM and *γ*-RCM

In *l*-RCM, two parameters are used to describe the process of OM degradation. The position of the peak point ln(μ) is the most important factor to control its distribution range. Compared with σ, the OM degradation curve is more sensitive to μ. Parameter μ plays a dominant role and determines the residual amount of OM after a period of time, while σ shape of the curve in a small range (Fig. S4) and larger value of σ means wider distribution of k.

Based on our fitting of 123 globally distributed OM data, as well as OM degradation in terrestrial soils and OM degradation in the laboratory, we found that the value of μ varies between 10^{-6} and 10 yr^{-1}, with the value of σ mainly concentrated between 0 and 6. According to the characteristics of the lognormal distribution, 95.45% of the area was within two standard deviations (2σ) of the mean left and right (Fig. S4). When σ equals 6, the reactivity distribution spans almost 12 orders of magnitude, which is sufficient to describe the composition of the different reactivity OM.

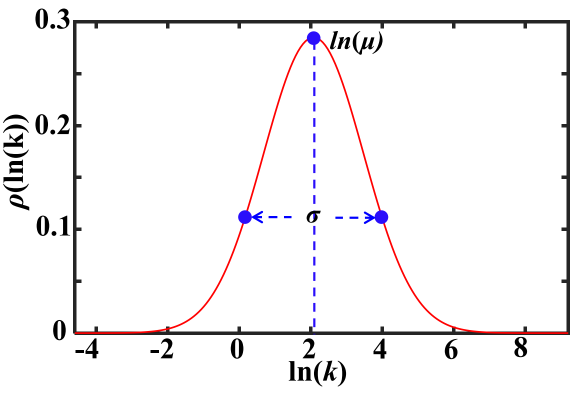

Fig. S4. Schematic diagram of lognormal distribution.

In *γ*-RCM, the parameter a was considered the key parameter and controlled the OM degradation process. However, we suggested that v is the most important parameter. First, v controls the shape of the gamma distribution, mathematically. When $v<1$, the gamma distribution is divergent and tends to infinity near 0. When $v \geqslant 1$, the gamma distribution is convergent (Fig. S5).

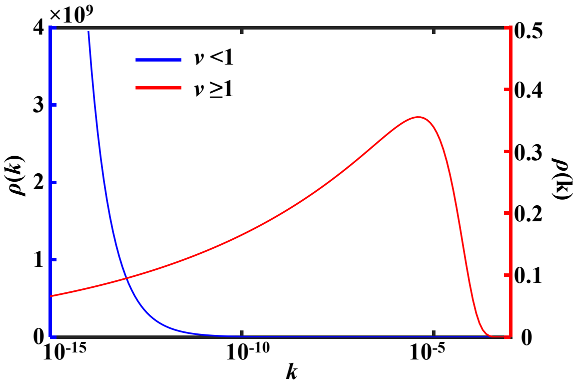

Fig. S5. Schematic diagram of gamma distribution.

Additionally, we did parameter sensitivity analysis for *γ*-RCM and *l*-RCM, respectively. The results shown that when v is fixed value, the parameter a can vary over a wide range (from 10000 to 20000) while maintaining a relatively good fit (R^2>0.9). However, when a is a fixed value, the variation of parameter v can cause a large fitting error. The results were shown in the Table S2 and Fig. S5. Besides, we found when both a and v had a huge change, *γ*-RCM can also obtain a good fit result, as shown in the Fig. S8.

Table S2. Fitting results of parametric sensitivity analysis of *γ*-RCM

Sensitivity analysis of *γ*-RCM							
BX-6	***v*=0.278**	*a*=12.5	R^2=0.82	**DSDP 58**	***v*=1.08**	*a*=10224	R^2=0.91
		a=22.5	R^2=0.93			*a*=12224	R^2=0.92
		a=32.5	R^2=0.86			*a*=14224	R^2=0.93
		a=42.5	R^2=0.74			*a*=16224	R^2=0.92
		a=52.5	R^2=0.61			*a*=18224	R^2=0.92
						a=20224	R^2=0.92
	***a*=22.5**	*v*=0.178	R^2=0.56		***a*=20224**	*v*=0.68	R^2=0.63
		v=0.278	R^2=0.93			*v*=0.88	R^2=0.84
		v=0.378	R^2=0.76			*v*=1.08	R^2=0.92
						v=1.28	R^2=0.93
						v=1.48	R^2=0.91

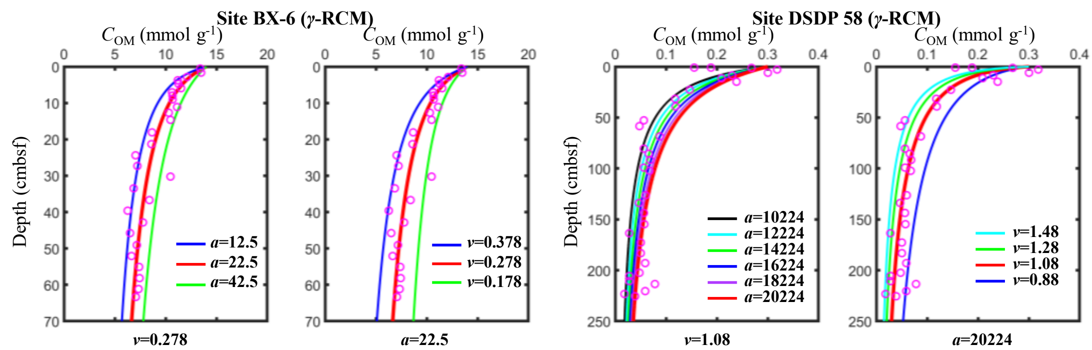

Fig. S6. Parameter sensitivity analysis of *γ*-RCM.

The *l*-RCM best-fit parameters are well fixed. According to the parametric sensitivity analysis, we found that very small changes in parameters μ and σ can cause large errors in the fitting results. The results were shown in the Table S3 and Fig. S7.

Table S3. Fitting results of parametric sensitivity analysis of *l*-RCM.

Sensitivity analysis of *l*-RCM							
BX-6	**μ=2.24 ×10^{-3}**	σ=1.031	R^2=0.71	**DSDP 58**	**μ=6.11 ×10^{-5}**	σ=0.663	R^2=0.87
		σ=2.031	R^2=0.93			σ=1.663	R^2=0.92
		σ=3.031	R^2=0.88			σ=2.663	R^2=0.88
		σ=4.031	R^2=0.83			σ=3.663	R^2=0.81
	σ=2.031	$\mu=1.24\times10^{-3}$	R^2=0.62		**σ=1.663**	$\mu=3.11\times10^{-5}$	R^2=0.86
		$\mu=2.24\times10^{-3}$	R^2=0.93			$\mu=6.11\times10^{-5}$	R^2=0.92
		$\mu=3.24\times10^{-3}$	R^2=0.89			$\mu=9.11\times10^{-5}$	R^2=0.87
		$\mu=4.24\times10^{-3}$	R^2=0.82			$\mu=12.11\times10^{-5}$	R^2=0.82

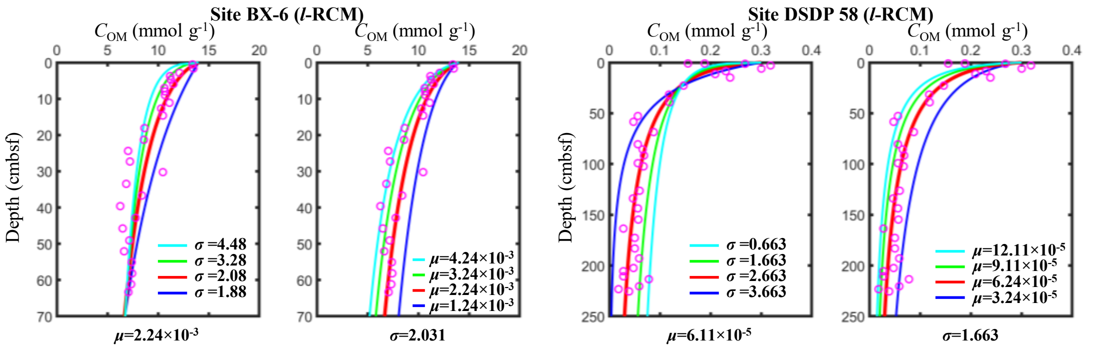

Fig. S7. Parameter sensitivity analysis of *l*-RCM.

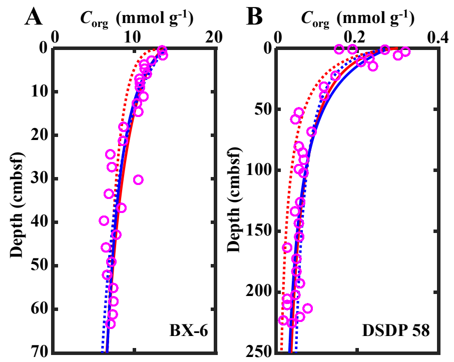

Fig. S8. A: pink circles are measured OM date. The red solid ($\mu=2.23\times10^{-3}$, σ=2.03, R^2=0.93) and dotted lines ($\mu=2.23\times10^{-3}$, σ=1.03, R^2=0.82) are the results of *l*-RCM, the blue solid (v=0.278, a=22.5, R^2=0.93) and dotted lines (v=0.5, a=53, R^2=0.91) are the results of γ-RCM. B: pink circles are measured OM date. The red solid ($\mu=6.11\times10^{-5}$, σ=1.66, R^2=0.92) and dotted lines ($\mu=8.8\times10^{-5}$, σ=1.36, R^2=0.78) are the results of *l*-RCM, the blue solid (v=1.08, a=20225, R^2=0.92) and dotted lines (v=0.5, a=4024, R^2=0.89) are the results of γ-RCM.

4. Distribution of regional OM reactivity at the SWI

If we consider the content of OM in regional or global surface sediments as a whole ($G_w(0)$), the degradation of OM on a regional or global scale can be reasonably assessed in combination with its reactivity distribution. The distribution of OM reactivity at the regional to global scale, $F(k,0)$, can be expressed as:

$$F(k,0)=\sum_{i=1}^{n}\frac{G_i(0)\cdot g_i(k,0)}{\sum_1^n G_i(0)} \tag{S2}$$

where $G_i(0)$ is the content of OM at the SWI of each grid cell ($\sum_i^n G_i(0)= G_w(0)$) and $g_i(k,0)$ is its reactivity distribution.

We collected data (including OM content in surface sediment and water depth) from 5,600 sites located in the global ocean (Fig. S11) (Seiter et al., 2004). First, we divided the ocean into 30 regions based on Seiter et al., (2004). According to the empirical relationship for μ, σ, sedimentation rate and water depth (Fig. S9 and S10), we obtained OM reactivity distribution within 5600 sites. Notably, the higher empirical relationship between OM reactivity and sedimentation rate (as black lines in Fig. S9 and S10) were applied in the EWTP, ARBS, NWAM and SWAF regions. Then, based on sites in different regions (Fig. S11), the distribution of the overall OM reactivity in different regions were obtained (Fig. S12). The higher and broader OM reactivity distributions were shown in the SWAF and NWAM regions, while they also have high mean TOC content in surface sediments, 2.5 wt.% and 1.7 wt.% (Table 1 in the main text), respectively. The ARBS region consists of 25% of shelf and 75% of abyss region, thus its overall reactivity distribution is smaller than the SWAF and NWAM regions. Despite the high mean TOC content (~1.21 wt.%) and reactivity of surface OM in the EWEP region, the relatively homogeneous source of OM makes its relatively narrow reactivity distribution.

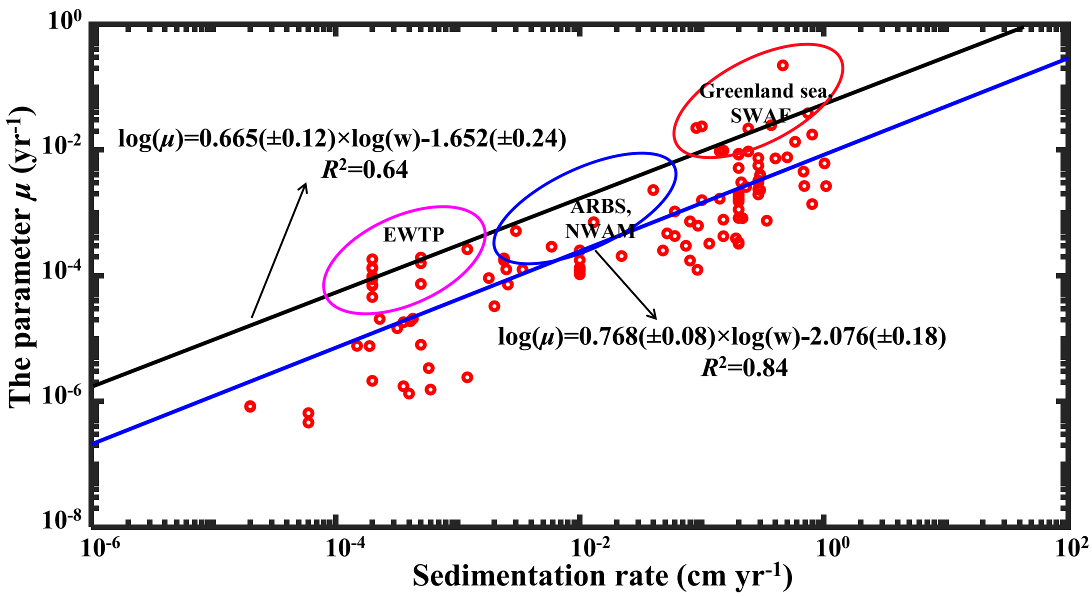

Fig. S9. The empirical relationship between sedimentation rate and μ in *l*-RCM. The red dots are the calculated values of μ, and the blue and black lines are the linear regression curve in the log-log coordinate system. The black line was used to calculate μ for sites in the EWTP, ARBS, NWAM and SWAF regions. The remaining sites were calculated using the blue line.

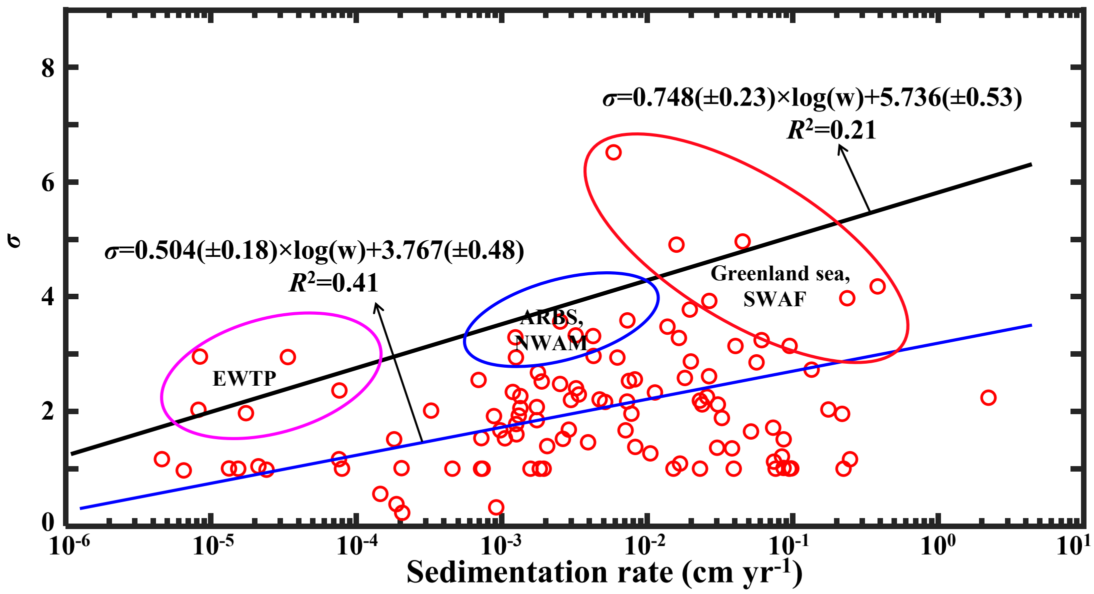

Fig. S10. The empirical relationship between sedimentation rate and σ in *l*-RCM. The red dots are the calculated values of σ, and the blue and black lines are the linear regression curve in the log-log coordinate system. The black line was used to calculate σ for sites in the EWTP, ARBS, NWAM and SWAF regions. The remaining sites were calculated using the blue line.

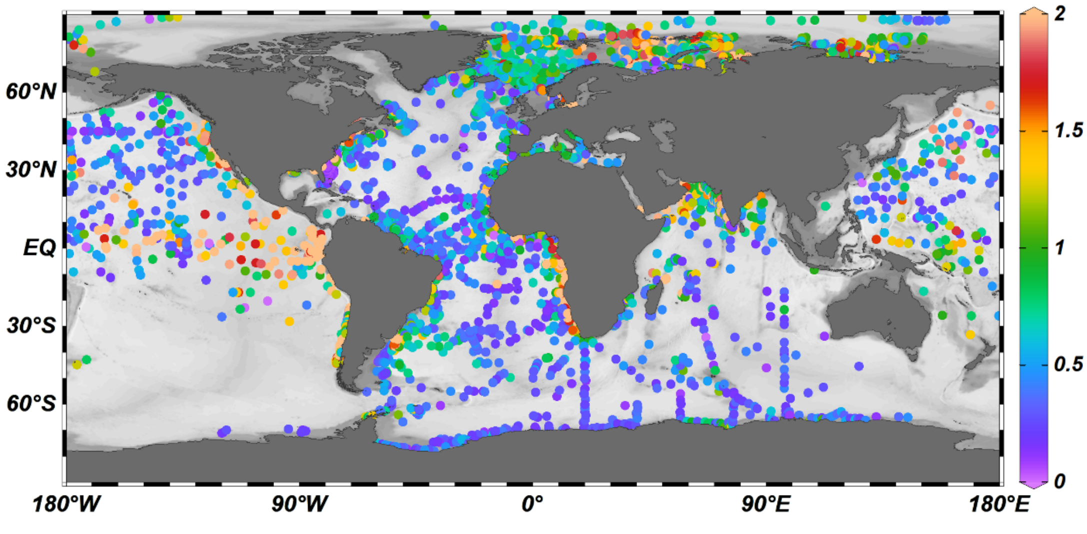

Fig. S11. Distribution of sites containing surface TOC content (wt.%). The shade of the circle color represents the magnitude of the TOC content.

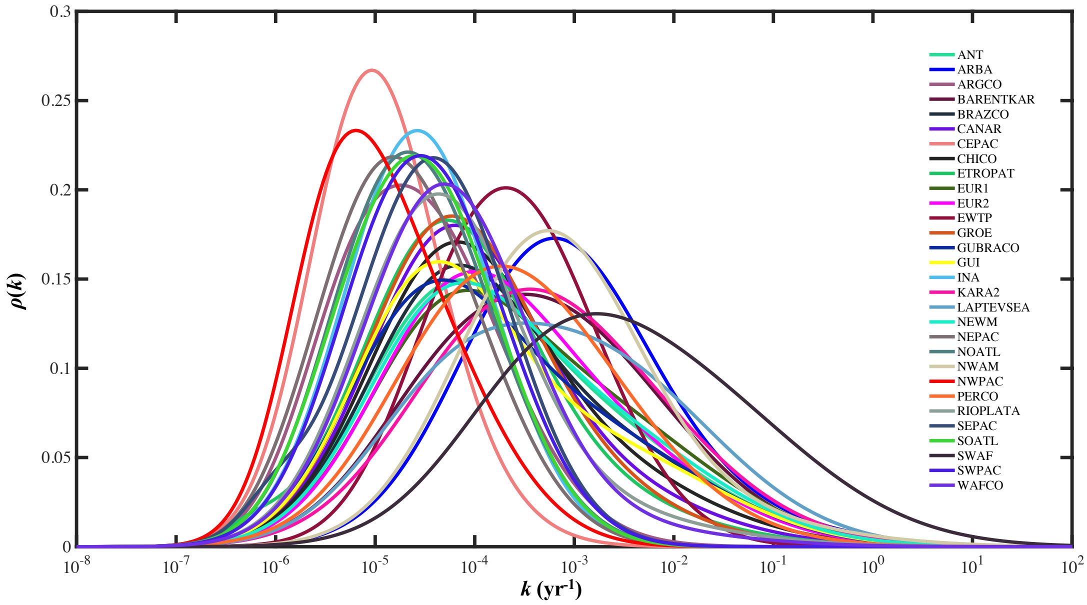

Fig. S12. OM reactivity distribution at the SWI in different regions.

5. Depth-integrated of OM degradation rate

Considering OM reactivity distribution at the SWI in each region ($F_i(k,0)$) is irregular distributions (Fig. S12), we divide the $F_i(k,0)$ into 1000 OM reactivity components, where the range of k is from 10^{-10} to 10^4 yr^{-1}. The middle part of equation (S3) can be written as:

$$< k >= \int_0^\infty k \cdot F_i(k,0)dk = \sum_{i=1}^{1000} f_i \cdot k_i \tag{S3}$$

where f_i is the fraction of each OM reactivity component. Statistically, the area covered under the distribution curve, $F_i(k,0)$, is constant at 1. When $1<i<1000$, as shown in the Fig. S13, $f_i=S_{i+1}/1$. When the distance between k_i and k_{i+1} is small enough (1000 components meet the requirements of calculation accuracy), the area of the irregular sector, S_{i+1}, can be expressed as the area of a small rectangle:

$$S_{i+1} \approx (k_{i+1} - k_i) \cdot (\rho(k_{i+1}) + \rho(k_i))/2 \tag{S4}$$

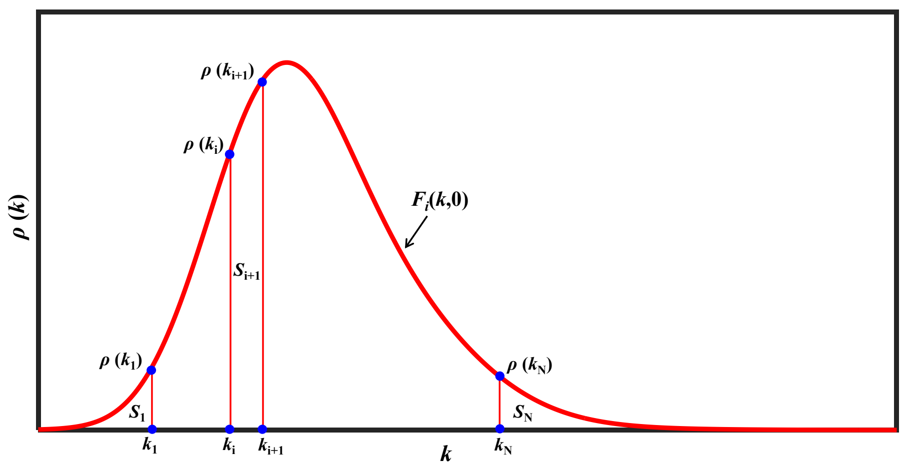

Fig. S13. Schematic diagram of the solution of equation (S5).

Combined with k_i, written as $k_i=(k_{i+1}+k_i)/2$, the intermediate component ($1<j<1000$) can be solved. When i=1 and 1000, $k_1=10^{-10}$ and $k_{1000}=10^4$ yr^{-1}. The sum of S ($1<i<1000$) equals 0.9999983 and we let $f_1=f_{1000}\approx$ (1-0.9999983)/2. According to this method and Fig. S12, we can calculate $<k_i>$ in each region, and the results of $<k_i>$ in each region are shown in the Table 1 in the main text.

Table S4. Supplementary sources of data for Fig. S1.

longitude	latitude	Sea area	Water depth	ω	G_{max}	Ref.
(°)	(°)	(*Ocean*)	(*m*)	(*cm/a*)	(*wt%*)	
72°45′ W	42°15′ N	Long Island Sound	10	0.2	1.7	(1)
131°75′ E	43°11′ N	Amur Bay	1	0.3	2.9	(29)
130°72′ E	42°61′ N	Ekspeditsii Bight	1.5	0.4	2.1	(29)
131°83′ E	42°96′ N	Voevoda bight	2.1	0.3	6.2	(29)
09°08′ E	56°53.10′ N	Livø Strait	7	0.1	6.2	(27)
04°18′ E	51°77′ N	Haringvliet Lake	7.5	1.01	4.73	(26)
123°29′ W	48°36′ N	NorthCarolina,USA	8	0.15	4.5	(9)
09°09′ E	56°50.32′ N	Bjørnsholm Bay	10	0.1	12	(27)
70°63′ W	41°73.8′ N	Buzzards Bay	15	0.2	1.9	(14)
70°62′ W	41°74.4′ N	Buzzards Bay	16	0.2	2.1	(14)
71°41′ W	41°43.9′ N	Rhode Island	17	0.2	16	(14)
89°44′ W	29°07′ N	Mississippi River	20	0.8	0.9	(22)
89°35′ W	29°06′ N	Mississippi River	20	0.8	0.52	(22)
73°42′ W	43°81′ S	Southern Chilean	20	0.29	1.4	(23)
73°51′ W	43°47′ S	Southern Chilean	20	0.29	3.2	(23)
73°63′ W	44°62′ S	Southern Chilean	20	0.29	3.1	(23)
73°18′ W	45°31′ S	Southern Chilean	20	0.29	1.6	(23)
74°46′ W	44°51′ S	Southern Chilean	20	0.29	2.4	(23)
74°53′ W	45°68′ S	Southern Chilean	20	0.29	1.5	(23)
13°86′ E	54°74′ N	Arkona Bassin	35	0.048	3.8	(21)
13°79′ E	54°80′ N	Arkona Bassin	44	0.074	4.1	(21)
13°66′ E	54°94′ N	Arkona Bassin	44	0.19	5.2	(21)
13°61′ E	54°91′ N	Arkona Bassin	44	0.215	4.9	(21)
136°78′ W	34°29′ N	Ago Bay	50	0.2	2.5	(18)
136°72′ W	34°30′ N	Ago Bay	50	0.2	2.4	(18)
136°70′ W	34°25′ N	Ago Bay	50	0.2	2.48	(18)
14°18′ E	23°46.52′ S	Namibian shelf	110	0.34	12	(16)
86°13′ W	09°37′ N	Costa Rica	160	0.01	2.4	(20)
86°11′ W	09°39′ N	Costa Rica	160	0.01	1.75	(20)
86°15′ W	09°42′ N	Costa Rica	160	0.01	1.6	(20)
123°25′ W	48°32′ N	Saanich Inlet	170	0.69	4.8	(7)
05°12′ W	78°93′ N	East Greenland shelf	189	0.37	0.72	(24)
12°77′ W	74°99′ N	East Greenland shelf	320	0.46	0.48	(24)
04°59′ W	75°06′ N	Central Greenland	272	0.09	0.62	(24)
123°30′ W	48°37′ N	Saanich Inlet	210	1.04	3.8	(11)
77°39′ W	12°0.5′ S	Peru continental	186	0.23	14	(2)

77°40′ W	12°0.5′ S	Peru continental	255	0.23	7.9	(2)
76°50′ W	13°37.3′ S	Peru continental	370	0.14	20	(5)
76°51′ W	13°37.3′ S	Peru continental	370	0.04	20	(5)
77°57′ W	11°15.1′ S	Peru continental	186	0.15	14	(5)
78°07′ W	11°20.6′ S	Peru continental	411	0.15	20	(4)
77°24′ W	12°23′ S	Peruvian margin	297	0.06	17.2	(33)
77°10′ W	12°13′ S	Peruvian margin	306	0.3	3.1	(33)
77°15′ W	12°17′ S	Peruvian margin	409	0.5	14.8	(33)
24°59′ W	71°21′ N	Weddell Sea	422	0.58	0.28	(25)
120°14′ W	34°19.3′ N	Santa Barbara Basin	430	0.2	2.8	(13)
120°01′ W	34°14.3′ N	Santa Barbara Basin	578	0.2	3.2	(13)
120°02′ W	34°16.0′ N	Santa Barbara Basin	585	0.2	2.6	(13)
12°85′ E	38°13′ N	Castellammare	550	0.2	1.1	(28)
12°91′ E	38°14′ N	Castellammare	550	0.2	0.85	(28)
146°00′ E	49°44.88′ N	Sea of Okhotsk	613	0.093	2.1	(30)
144°04′ E	54°26.52′ N	Sea of Okhotsk	685	0.022	1.7	(30)
144°42′ E	52°43.88′ N	Sea of Okhotsk	713	0.115	1.8	(30)
144°14′ E	53°50.00′ N	Sea of Okhotsk	771	0.092	1.7	(30)
146°02′ E	48°22.73′ N	Sea of Okhotsk	1256	0.013	1.6	(30)
146°08′ E	48°11.83′ N	Sea of Okhotsk	1602	0.01	0.83	(30)
77°11′ W	12°14′ S	Peruvian margin	695	0.3	6.1	(33)
77°35′ W	12°31′ S	Peruvian margin	756	0.08	2.9	(33)
77°40′ W	12°35′ S	Peruvian margin	770	0.052	4.6	(33)
02°45′ W	62°79′ N	Shetland Faeroe	777	0.68	1.2	(24)
119°42′ E	22°29′ N	South China Sea	1004	0.08	0.78	(32)
38°51′ W	77°39′ N	Weddell Sea	1097	0.21	0.42	(25)
31°24′ W	74°24′ N	Weddell Sea	1178	0.14	0.36	(25)
09°67′ W	68°71′ N	Weddell Sea	1185	0.08	0.32	(25)
27°64′ W	73°17′ N	Weddell Sea	1566	0.24	0.35	(25)
22°36′ W	73°36′ N	Weddell Sea	1598	0.24	0.25	(25)
27°16′ W	73°48′ N	Weddell Sea	444	0.74	0.21	(25)
118°83′ W	32°85′ N	Southern California	1500	0.06	6.5	(23)
65°35′ E	20°00′ N	Arabian Sea	3000	0.0024	0.56	(31)
68°33′ E	15°36′ N	Arabian Sea	3500	0.0025	0.95	(31)
64°33′ E	14°24′ N	Arabian Sea	3500	0.0024	0.63	(31)
65°02′ E	10°03′ N	Arabian Sea	3500	0.0012	0.53	(31)
60°31′ E	16°10′ N	Arabian Sea	4000	0.0034	3.8	(31)
71°24′ W	36°10′ N	NW Atlantic	4215	0.01	1.2	(8)
70°50′ W	32°59.3′ N	NW Atlantic	4595	0.003	0.28	(8)
60°50′ W	35°19.8′ N	NW Atlantic	5341	0.01	0.34	(8)
136°03′ E	28°59.00′ N	Philippine Sea	2972	0.00006	0.34	(6)
135°93′ E	29°08.00′ N	Shikoku Basin	2972	0.00006	0.5	(6)
135°99′ E	29°10.00′ N	Shikoku Basin	2972	0.00006	0.42	(6)
134°93′ E	28°59.00′ N	Shikoku Basin	2972	0.00002	0.27	(6)

151°39′ W	13°41.7′ N	the North Pacific	5686	0.00015	0.4	(10)
148°57′ W	6°13.2′ N	the North Pacific	5718	0.00019	0.23	(10)
146°09′ W	9°30.5′ N	the North Pacific	5004	0.00023	0.36	(10)
146°01′ W	9°19.3′ N	the North Pacific	5205	0.00032	0.45	(10)
145°59′ W	9°31.5′ N	the North Pacific	5164	0.00036	0.26	(10)
144°49′ W	3°59.5′ N	the North Pacific	5214	0.00036	0.22	(10)
145°01′ W	3°50.2′ N	the North Pacific	4599	0.00041	0.23	(10)
148°44′ W	9°15.0′ N	the North Pacific	4619	0.00043	0.35	(10)
148°46′ W	9°06.5′ N	the North Pacific	5144	0.00058	0.32	(10)
151°39′ W	14°41.7′ N	the North Pacific	5686	0.0002	0.2	(10)
148°47′ W	9°06.5′ N	the North Pacific	5189	0.0012	0.25	(10)
168°46′ W	65°01.7′ S	South flank Pacific	2930	0.00258	0.5	(12)
174°14′ W	66°49.7′ S	South flank Pacific	3260	0.0018	0.32	(12)
174°44′ W	62°54.2′ S	North flank Pacific	4139	0.00588	0.6	(12)
63°27′ W	22°54.9′ N	Nares Abyssal Plain	5868	0.0005	0.3	(15)
63°26′ W	22°54.9′ N	Nares Abyssal Plain	5868	0.0005	0.14	(15)
63°00′ W	23°22.3′ N	Nares Abyssal Plain	5878	0.0005	0.12	(15)
63°01′ W	23°22.3′ N	Nares Abyssal Plain	5878	0.0005	0.008	(15)
169°04′ E	08°13′ N	Equatorial Pacific	4239	<0.002	0.25	(17)
177°58′ E	07°27′ N	Equatorial Pacific	5269	<0.002	0.42	(17)
175°52′ W	05°03′ N	Equatorial Pacific	5867	<0.002	0.6	(17)
174°54′ W	03°04′ N	Equatorial Pacific	3572	<0.002	0.54	(17)
171°04′ W	00°02′ S	Equatorial Pacific	5352	<0.002	0.7	(17)
168°04′ W	02°26′ S	Equatorial Pacific	5361	<0.002	0.52	(17)
166°37′ W	03°39′ S	Equatorial Pacific	5469	<0.002	0.53	(17)
166°32′ W	09°10′ S	Equatorial Pacific	5283	<0.002	0.15	(17)
85°22′ W	05°30′ S	Peru Basin	4082	0.002	1.7	(19)
85°11′ W	06°34′ S	Peru Basin	4165	0.0006	0.72	(19)
88°27′ W	07°40′ S	Peru Basin	4127	0.0004	0.8	(19)
3.07 W	51.5 N	Severn estuary	8	0.43	2.9	(34)
4.85 E	43.31 N	Rhone zone	19	0.1	1.9	(35)
4.77 E	43.27 N	Rhone shelf	74	0.5	1.5	(36)
10.34 E	56.11 N	Aarhus Bay	15	0.32	3.8	(37)
13.78 E	54.8 N	Arkona Basin	43	0.0074	3.9	(38)
7.97 E	54.08 N	Helgoland Mud	29	1.3	1.1	(39)
9.75 E	57.92 N	Skagerrak S10	86	0.5	1.4	(40)
9.7 E	57.95 N	Skagerrak S11	150	0.5	0.7	(41)
9.6 E	58.05 N	Skagerrak S13	386	0.5	2.1	(42)
63.02 E	24.88 N	Arabian Sea	645	0.05	1.1	(43)
62.99 E	24.81 N	Arabian Sea	957	0.05	0.95	(44)
62.99 E	24.71 N	Arabian Sea	1586	0.05	0.92	(45)
168.8 W	54.57 N	Bering Sea	1476	0.0016	1.6	(46)
53.59 W	39.31 S	Argentine Basin	3687	0.008	1.2	(47)

Reference for supplementary Table 4

[1] Goldhaber, M. B., Aller, R. C., Cochran, J. K., Rosenfeld, J. K., Martens, C. S., & Berner, R. A. (1977). Sulfate reduction, diffusion, and bioturbation in Long Island Sound sediments; report of the FOAM Group. American Journal of Science, 277(3), 193-237.

[2] Froelich, P. N., Arthur, M. A., Burnett, W. C., Deakin, M., Hensley, V., Jahnke, R., ... & Vathakanon, C. (1988). Early diagenesis of organic matter in Peru continental margin sediments: phosphorite precipitation. Marine Geology, 80(3-4), 309-343.

[3] Müller, P. J., & Mangini, A. (1980). Organic carbon decomposition rates in sediments of the Pacific manganese nodule belt dated by 230Th and 231Pa. Earth and planetary science letters, 51(1), 94-114.

[4] Reimers, C. E. (1982). Organic matter in anoxic sediments off central Peru: relations of porosity, microbial decomposition and deformation properties. Marine Geology, 46(3-4), 175-197.

[5] Reimers, C. E., & Suess, E. (1983). The partitioning of organic carbon fluxes and sedimentary organic matter decomposition rates in the ocean. Marine Chemistry, 13(2), 141-168.

[6] Waples, D. W., & Sloan, J. R. (1980). Carbon and nitrogen diagenesis in deep sea sediments. Geochimica et Cosmochimica Acta, 44(10), 1463-1470.

[7] Hamilton, S. E., & Hedges, J. I. (1988). The comparative geochemistries of lignins and carbohydrates in an anoxic fjord. Geochimica et Cosmochimica Acta, 52(1), 129-142.

[8] Heggie, D., Maris, C., Hudson, A., Dymond, J., Beach, R., & Cullen, J. (1987). Organic carbon oxidation and preservation in NW Atlantic continental margin sediments. Geological Society, London, Special Publications, 31(1), 215-236.

[9] Martens, C. S., & Klump, J. V. (1984). Biogeochemical cycling in an organic-rich coastal marine basin 4. An organic carbon budget for sediments dominated by sulfate reduction and methanogenesis. Geochimica et Cosmochimica Acta, 48(10), 1987-2004.

[10] Müller, P. J., & Mangini, A. (1980). Organic carbon decomposition rates in sediments of the Pacific manganese nodule belt dated by 230Th and 231Pa. Earth and planetary science letters, 51(1), 94-114.

[11] Murray, J. W., Grundmanis, V., & Smethie Jr, W. M. (1978). Interstitial water chemistry in the sediments of Saanich Inlet. Geochimica et Cosmochimica Acta, 42(7), 1011-1026.

[12] Reimers, C. E., & Suess, E. (1983). The partitioning of organic carbon fluxes and sedimentary organic matter decomposition rates in the ocean. Marine Chemistry, 13(2), 141-168.

[13] Sholkovitz, E. (1973). Interstitial water chemistry of the Santa Barbara Basin sediments. Geochimica et Cosmochimica Acta, 37(9), 2043-2073.

[14] Henrichs, S. M., & Farrington, J. W. (1987). Early diagenesis of amino acids and organic matter in two coastal marine sediments. Geochimica et Cosmochimica Acta, 51(1), 1-15.

[15] Thomson, J., Higgs, N. C., & Colley, S. (1989). A geochemical investigation of reduction haloes developed under turbidites in brown clay. Marine geology, 89(3-4), 315-330.

[16] Dale, A. W., Brüchert, V., Alperin, M., & Regnier, P. (2009). An integrated sulfur isotope model for Namibian shelf sediments. Geochimica et Cosmochimica Acta, 73(7), 1924-1944.

[17] Grundmanis, V., & Murray, J. W. (1982). Aerobic respiration in pelagic marine sediments. Geochimica et Cosmochimica Acta, 46(6), 1101-1120.

[18] Kasih, G. A., Chiba, S., Yamagata, Y., Shimizu, Y., & Haraguchi, K. (2008). Modeling early diagenesis of sediment in Ago Bay, Japan: A comparison of steady state and dynamic calculations. Ecological modelling, 215(1-3), 40-54.

[19] Haeckel, M., König, I., Riech, V., Weber, M. E., & Suess, E. (2001). Pore water profiles and numerical modelling of biogeochemical processes in Peru Basin deep-sea sediments. Deep Sea Research Part II: Topical Studies in Oceanography, 48(17-18), 3713-3736.

[20] Hensen, C., & Wallmann, K. (2005). Methane formation at Costa Rica continental margin—constraints for gas hydrate inventories and cross-décollement fluid flow. Earth and Planetary Science Letters, 236(1-2), 41-60.

[21] Mogollón, J. M., Dale, A. W., Fossing, H., & Regnier, P. (2012). Timescales for the development of methanogenesis and free gas layers in recently-deposited sediments of Arkona Basin (Baltic Sea). Biogeosciences (BG), 9, 1915-1933.

[22] Morse, J. W., & Eldridge, P. M. (2007). A non-steady state diagenetic model for changes in sediment biogeochemistry in response to seasonally hypoxic/anoxic conditions in the "dead zone" of the Louisiana shelf. Marine Chemistry, 106(1-2), 239-255.

[23] Rojas, N., & Silva, N. (2005). Early diagenesis and vertical distribution of organic carbon and total nitrogen in recent sediments from southern Chilean fjords (Boca del Guafo to Pulluche Channel). Investigaciones marinas, 33(2), 183-194.

[24] Sauter, E. J., Schlüter, M., & Suess, E. (2001). Organic carbon flux and remineralization in surface sediments from the northern North Atlantic derived from pore-water oxygen microprofiles. Deep Sea Research Part I: Oceanographic Research Papers, 48(2), 529-553.

[25] Schlüter, M. (1991). Organic carbon flux and oxygen penetration into sediments of the Weddell Sea: indicators for regional differences in export production. Marine chemistry, 35(1-4), 569-579.

[26] Canavan, R. W., Slomp, C. P., Jourabchi, P., Van Cappellen, P., Laverman, A. M., & Van den Berg, G. A. (2006). Organic matter mineralization in sediment of a coastal freshwater lake and response to salinization. Geochimica et Cosmochimica Acta, 70(11), 2836-2855.

[27] Jørgensen, B. B., JØrgensen, B. B., & Parkes, R. J. (2010). Role of sulfate reduction and methane production by organic carbon degradation in eutrophic fjord sediments (Limfjorden, Denmark). Limnology and Oceanography, 55(3), 1338-1352.

[28] Paradis, S., Pusceddu, A., Masqué, P., Puig, P., Moccia, D., Russo, T., & Iacono, C. L. (2019). Organic matter contents and degradation in a highly trawled area during fresh particle inputs (Gulf of Castellammare, southwestern Mediterranean).

[29] Tishchenko, P. Y., Medvedev, E. V., Barabanshchikov, Y. A., Pavlova, G. Y., Sagalaev, S. G., Tishchenko, P. P., ... & Orekhova, N. A. (2020). Organic Carbon and Carbonate System in the Bottom Sediments of Shallow Bights of the Peter the Great Bay (Sea of Japan). Geochemistry International, 58(6), 704-718.

[30] Wallmann, K., Aloisi, G., Haeckel, M., Obzhirov, A., Pavlova, G., & Tishchenko, P. (2006). Kinetics of organic matter degradation, microbial methane generation, and gas hydrate formation in anoxic marine sediments. Geochimica et Cosmochimica Acta, 70(15), 3905-3927.

[31] Luff, R., Wallmann, K., Grandel, S., & Schlüter, M. (2000). Numerical modeling of benthic processes in the deep Arabian Sea. Deep Sea Research Part II: Topical Studies in Oceanography, 47(14), 3039-3072.

[32] Chuang, P. C., Yang, T. F., Wallmann, K., Matsumoto, R., Hu, C. Y., Chen, H. W., ... & Dale, A. W. (2019). Carbon isotope exchange during anaerobic oxidation of methane (AOM) in sediments of the northeastern South China Sea. Geochimica et Cosmochimica Acta, 246, 138-155.

[33] Dale, A. W., Sommer, S., Lomnitz, U., Montes, I., Treude, T., Liebetrau, V., ... & Bryant, L. D. (2015). Organic carbon production, mineralization and preservation on the Peruvian margin.

Biogeosciences (BG), 12, 1537-1559.

[34] Langston, W. J., Pope, N. D., Jonas, P. J. C., Nikitic, C., Field, M. D. R., Dowell, B., ... & Brown, A. R. (2010). Contaminants in fine sediments and their consequences for biota of the Severn Estuary. Marine Pollution Bulletin, 61(1-3), 68-82.

[35] Pastor, L., Deflandre, B., Viollier, E., Cathalot, C., Metzger, E., Rabouille, C., ... & Grémare, A. (2011). Influence of the organic matter composition on benthic oxygen demand in the Rhône River prodelta (NW Mediterranean Sea). Continental Shelf Research, 31(9), 1008-1019.

[36] Aquilina, A., Knab, N. J., Knittel, K., Kaur, G., Geissler, A., Kelly, S. P., ... & Pancost, R. D. (2010). Biomarker indicators for anaerobic oxidizers of methane in brackish-marine sediments with diffusive methane fluxes. Organic Geochemistry, 41(4), 414-426.

[37] Thingstad, T. F., Riemann, B. O., Havskum, H., & Garde, K. (1996). Incorporation rates and biomass content of C and P in phytoplankton and bacteria in the Bay of Aarhus (Denmark) June 1992. Journal of plankton research, 18(1), 97-121.

[38] Fleming, V., & Kaitala, S. (2006). Phytoplankton spring bloom intensity index for the Baltic Sea estimated for the years 1992 to 2004. Hydrobiologia, 554(1), 57-65.

[39] Hebbeln, D., Scheurle, C., & Lamy, F. (2003). Depositional history of the Helgoland mud area, German Bight, North Sea. Geo-Marine Letters, 23(2), 81-90.

[40] Dahl, E., & Johannessen, T. (1998). Temporal and spatial variability of phytoplankton and chlorophyll a: lessons from the south coast of Norway and the Skagerrak. ICES Journal of Marine Science, 55(4), 680-687.

[41] Richardson, K., Rasmussen, B., Bunk, T., & Mouritsen, L. T. (2003). Multiple subsurface phytoplankton blooms occurring simultaneously in the Skagerrak. Journal of plankton research, 25(7), 799-813.

[42] Trimmer, M., Engström, P., & Thamdrup, B. (2013). Stark contrast in denitrification and anammox across the deep Norwegian trench in the Skagerrak. Applied and environmental microbiology, 79(23), 7381-7389.

[43] Bard, E., Ménot, G., Rostek, F., Licari, L., Böning, P., Edwards, R. L., ... & Heaton, T. J. (2013). Radiocarbon calibration/comparison records based on marine sediments from the Pakistan and Iberian margins. Radiocarbon, 55(4), 1999-2019.

[44] Barlow, R. G., Mantoura, R. F. C., & Cummings, D. G. (1999). Monsoonal influence on the distribution of phytoplankton pigments in the Arabian Sea. Deep Sea Research Part II: Topical Studies in Oceanography, 46(3-4), 677-699.

[45] Koho, K. A., Nierop, K. G. J., Moodley, L., Middelburg, J. J., Pozzato, L., Soetaert, K., ... & Reichart, G. J. (2013). Microbial bioavailability regulates organic matter preservation in marine sediments. Biogeosciences, 10, 1131-1141.

[46] Coyle, K. O., Pinchuk, A. I., Eisner, L. B., & Napp, J. M. (2008). Zooplankton species composition, abundance and biomass on the eastern Bering Sea shelf during summer: the potential role of water-column stability and nutrients in structuring the zooplankton community. Deep Sea Research Part II: Topical Studies in Oceanography, 55(16-17), 1775-1791.

[47] Benthien, A., & Müller, P. J. (2000). Anomalously low alkenone temperatures caused by lateral particle and sediment transport in the Malvinas Current region, western Argentine Basin. Deep Sea Research Part I: Oceanographic Research Papers, 47(12), 2369-2393.

References

Arndt, S., Jørgensen, B. B., LaRowe, D. E., Middelburg, J., Pancost, R., and Regnier, P., 2013, Quantifying the degradation of organic matter in marine sediments: a review and synthesis: Earth-science reviews, v. 123, p. 53-86.

Betts, J., and Holland, H., 1991, The oxygen content of ocean bottom waters, the burial efficiency of organic carbon, and the regulation of atmospheric oxygen: Palaeogeography, Palaeoclimatology, Palaeoecology, v. 97, no. 1-2, p. 5-18.

Boudreau, B. P., and Ruddick, B. R., 1991, On a reactive continuum representation of organic matter diagenesis: American Journal of Science, v. 291, no. 5, p. 507-538.

Burwicz, E. B., Rüpke, L., and Wallmann, K., 2011, Estimation of the global amount of submarine gas hydrates formed via microbial methane formation based on numerical reaction-transport modeling and a novel parameterization of Holocene sedimentation: Geochimica et Cosmochimica Acta, v. 75, no. 16, p. 4562-4576.

Colman, A. S., and Holland, H. D., 2000, The global diagenetic flux of phosphorus from marine sediments to the oceans: redox sensitivity and the control of atmospheric oxygen levels.

Egger, M., Riedinger, N., Mogollón, J. M., and Jørgensen, B. B., 2018, Global diffusive fluxes of methane in marine sediments: Nature Geoscience, v. 11, no. 6, p. 421-425.

Seiter, K., Hensen, C., Schröter, J., and Zabel, M., 2004, Organic carbon content in surface sediments—defining regional provinces: Deep Sea Research Part I: Oceanographic Research Papers, v. 51, no. 12, p. 2001-2026.